JPhys Energy

PAPER • OPEN ACCESS

Understanding the dopability of p-type $Mg_2(Si,Sn)$ by relating hybrid-density functional calculation results to experimental data

To cite this article: Hasbuna Kamila *et al* 2022 *J. Phys. Energy* **4** 035001

View the article online for updates and enhancements.

You may also like

- Facile Synthesis and Electrochemistry of Si-Sn-C Nanocomposites for High-Energy Li-Ion Batteries
Jing Xu, Min Ling, Lydia Terborg et al.

- Fine-Grained Si Alloy Prepared By Melt Spinning and Its Electrochemical Performance for Li Ion Battery Anode
Tomohiro Kaburagi, Fumihiro Miki, Manabu Watanabe et al.

- A QuasiChemical Equilibrium Calculation of the GeSiSn and GeSiPb Ternary Phase Diagrams
G. B. Stringfellow and P. E. Greene

This content was downloaded from IP address 129.247.247.240 on 01/06/2022 at 13:16

IOP Publishing J. Phys. Energy 4 (2022) 035001 https://doi.org/10.1088/2515-7655/ac689d

Journal of Physics: Energy

OPEN ACCESS

RECEIVED
11 February 2022

REVISED
5 April 2022

ACCEPTED FOR PUBLICATION
20 April 2022

PUBLISHED
1 June 2022

Original content from this work may be used under the terms of the Creative Commons Attribution 4.0 licence.

Any further distribution of this work must maintain attribution to the author(s) and the title of the work, journal citation and DOI.

PAPER

Understanding the dopability of p-type Mg_2(Si,Sn) by relating hybrid-density functional calculation results to experimental data

Hasbuna Kamila[1,*], Byungki Ryu[2], Sahar Ayachi[1], Aryan Sankhla[1], Eckhard Mueller[1,3] and Johannes de Boor[1,4,*]

[1] German Aerospace Center (DLR), Institute of Materials Research, D–51147 Koeln, Germany
[2] Energy Conversion Research Center, Electrical Materials Research Division, Korea Electrotechnology Research Institute (KERI), Changwon 51543, Republic of Korea
[3] Justus Liebig University Giessen, Institute of Inorganic and Analytical Chemistry, D–35392 Giessen, Germany
[4] University of Duisburg–Essen, Institute of Technology for Nanostructures (NST), D–47057 Duisburg, Germany
[*] Authors to whom any correspondence should be addressed.

E-mail: hasbuna.kamila@dlr.de and Johannes.deboor@dlr.de

Keywords: dopability, p-types, Mg2(Si, Sn), single parabolic band model, Li-doped Mg2(Si, Sn), Hybrid-DFT, carrier concentration

Supplementary material for this article is available online

Abstract

It is crucial to reach a sufficiently high carrier concentration in order to optimize the thermoelectric (TE) material in the development of Mg_2X (X = Si, Ge, and Sn)-based TE generators. While n-type Mg_2(Si,Sn) has excellent TE properties, p-type shows suboptimal TE performance because of insufficient carrier concentration, in particular for Mg_2Si and Si-rich Mg_2(Si,Sn). A systematic investigation of Li-doped $Mg_2Si_{1-x}Sn_x$ has been performed as Li, in contrast to other typical dopants, has a high solubility in the material system and has been shown to yield the highest reported carrier concentrations. We observe that the carrier concentration increases with Li content, but the dopant efficiency decreases. With respect to the Si:Sn ratio, we find a clear increase in maximum achievable carrier concentration and dopant efficiency with increasing Sn content. The trends can be understood by employing defect formation energies obtained within the hybrid-density functional theory (DFT) for the binaries. Further, we use a linear interpolation of the hybrid-DFT results from the binaries to the ternary Mg_2(Si,Sn) compositions and a simple single parabolic band model to predict the maximal achievable carrier concentration for the solid solutions, providing a simple guideline for experimental work. Finally, we show that the approach is transferable to other material classes. This work highlights that, besides dopant solubility, the interplay between intrinsic and extrinsic defects determines the achievable carrier concentration.

1. Introduction

Mg_2X (X = Si, Ge, Sn) binaries and their solid solutions are among the most attractive thermoelectric (TE) materials for TE generators (TEGs) due to the high performance of n-type Mg_2(Si, Ge, Sn). This is expressed by a high figure of merit, $zT = 1.3$ [1–5], with the TE figure of merit defined as $zT = \frac{S^2\sigma}{k}T$, where S is the Seebeck coefficient, σ is the electrical conductivity, κ is the thermal conductivity, and T is the absolute temperature. All TE transport properties are sensitiveto the carrier concentration which needs to be adjusted to maximize zT. However, p-type Mg_2(Si,Sn) shows inferior TE properties to that of the corresponding n-type materials [6–8], partially due to a less favorable electronic band structure (low valley degeneracy and no band convergence) and partially due to the limited practically achievable carrier concentration (p), which is too low to maximize the TE performance. This is definitely true for compositions with Si < 0.5, but might even be valid for the optimum composition of $Mg_2Si_{0.4}Sn_{0.6}$ [3, 9]. Thus, it is crucial to reach a sufficiently high carrier concentration in order to optimize p-type Mg_2(Si, Sn) and be able to build high-performing TEG based on magnesium silicide. This is desirable as employing the same material class for both n- and p-type could reduce the considerable chemical complexity in the contact development [10] and avoid

© 2022 The Author(s). Published by IOP Publishing Ltd

mismatch of the coefficient of thermal expansion between the p- and n-type legs in TEG [11], thus making p-type Mg_2(Si,Sn) a promising candidate for pairing with n-type Mg_2(Si,Sn) for TEG application [12].

The maximum carrier concentration (p_{max}) is often limited by the solubility of the dopants. In the case of n-type Mg_2X, Bi and Sb are the best known dopants; for these it seems that the dopant solubility and the dopant efficiency are high enough to reach and exceed the optimum carrier concentration [13–16]. On the other hand, for p-type Mg_2X [6], employing Ag as a dopant has led to the formation of secondary phases such as MgAg [17–20]; the observed differences in phase constitution highlight that the solubility limit might interact with coexisting secondary phases. Furthermore, Na and Ga also exhibit low solubilities leading to the formation of secondary phases [21, 22]. For Li, however, which has led to the highest reported carrier concentrations [6, 21], the solubility was reported to be high, up to $Mg_{1.75}Li_{0.25}Si$ [23]. However, it has been speculated that Li might not only substitute Mg but also go on the interstitial position [24]. This is in agreement with density functional theory (DFT) calculations on the binaries, indicating a compensation between Li_{Mg} and Li_{int} [25, 26].

Hirayama *et al* [26] reported calculation results on neutral Li defects in Mg_2Si using the generalized gradient approximation (GGA). The result shows that Li goes preferably onto the Mg and interstitial sites as these have the lowest defect formation energy. As a Li substitutional at a Mg site (Li_{Mg}) is an acceptor defect but Li interstitial (Li_{int}) a donor defect this will generate holes and electrons simultaneously, making it difficult to achieve high p-type doping in Mg_2Si. More recently, Ayachi *et al* [25] presented defect formation energies of Li-related defects in Mg_2Si and Mg_2Sn calculated using hybrid-DFT. Furthermore, Ryu *et al* found that the band gap correction is crucial for defect physics and chemistry in these systems [27]. Similarly, previous publications show that Li goes into both sites (Mg and interstitial) even though the pre-assumptions were different (Hirayama *et al* did not consider charged defects) [25, 26].

Here, we summarize experimental results on the dependence of the carrier concentration on the Si:Sn ratio and Li dopant concentration. All samples have been prepared using the same synthesis method to reach a high degree of comparability. Charged defect formation energies by hybrid-DFT are used to predict the maximum achievable carrier concentation for Li-doped Mg_2Si and Mg_2Sn, and the predictions are compared with experimental values. We furthermore show that a linear interpolation of the hybrid-DFT results from the binaries to the ternary Mg_2(Si,Sn) compositions, and a relatively simple approach using a single parabolic band (SPB) model, are well suited to predicting the maximal achievable carrier concentration for the solid solutions, achieving good agreement with the experimental data. The approach is not restricted to Mg_2(Si,Sn); instead, the usefulness of combining defect energy calculations from DFT with a SPB model is demonstrated also for the PbSe and Mg_3Sb_2 systems.

2. Materials and methods

2.1. Sample preparation and characterization

Li-doped $Mg_2Si_{1-x}Sn_x$ samples were synthesized using a two-step synthesis method: high energy ball milling and current-assisted sintering, as described in our previous work [8, 28], without providing Mg excess as is often done in a melting route. The chosen sintering temperature depends on the composition, varies between 873 K for Mg_2Sn and 1073 K for Mg_2Si, respectively [8, 28], and is listed together with the measured carrier concentration in [29]. Note that all samples were found to be single phase and with similar microstructure, as discussed in [28, 30]. The only exception was Mg_2Sn which showed a minor impurity of Sn. For this reason, a possible influence of the microstructure is largely disregarded in the following. The room temperature Hall coefficient R_H was determined using an in-house facility with a van der Pauw configuration under a magnetic field sweep up to a maximum of 0.5 T. The carrier concentration p was estimated using the experimental R_H assuming a single carrier type; this is a reasonable estimation even for low doped Si-rich samples, as discussed in [29]. Note that the basic TE transport data of the samples was already published in [8, 28, 29].

The dopant efficiency was calculated from the obtained carrier concentration and the added dopant concentration under the assumption that each Li atom replaces one Mg atom and provides one free hole ($\frac{p}{c_{Li}}$; $c_{Li} = \frac{4\times \text{Li concentration}}{a^3}$ where a is the lattice parameter and 4 is the number of substitution sites for Li in the conventional cubic unit cell of a^3) as given in [28].

2.2. Hybrid-DFT calculations for charged defect formation energies and carrier density

First-principles calculations were conducted to investigate the defect properties of intrinsic and extrinsic defects in Mg_2Si and Mg_2Sn based on hybrid-DFT calculations within the HSE hybrid exchange correlation functional (HSE06) [31], following previous approaches [25, 27].

All the calculations of total energy and charged defect formation energy were performed using a Vienna *Ab Initio* Simulation Package code [32, 33]. The hybrid exchange correlation energy function of HSE06 was used with the exact-exchange mixing parameter of 25% and the screening parameter of 0.208 Å^{-1} with the

GGA parameterized by Perdew, Burke, and Ernzerhof [34]. We have chosen the exact-exchange mixing parameter of 25% as this has been employed successfully for this and other material systems [31]. We also note that a different choice influences the defect formation energies only very slightly. Projector-augmented wave pseudopotentials were used for atomic potentials. The plane-wave energy basis set was employed with the energy cut-off of 296 eV. Using a higher cut-off energy of 400 eV results in a change of <1 meV for the defect formation energies (see tables S2 and S4 in SI available online at stacks.iop.org/JPEnergy/4/035001/mmedia), showing a successful convergence of the calculations.

Mg_2Si and Mg_2Sn crystallize in the antifluorite structure (Space Group No. 225, Fm$\bar{3}$ m) as displayed in [26, 35]. Mg atoms occupy the 8c site while Si/Sn atoms occupy the 4a site. A defective system was modeled using a ($2 \times 2 \times 2$) cubic supercell with the lattice parameters of 12.7 Å and 13.5 Å for Mg_2Si and Mg_2Sn, respectively. In the supercell, there are 96 atoms consisting of 64 Mg and 32 Si/Sn atoms. The dopant atom is added, removed, or replaced in the host supercell to generate defective supercells for substitutional, vacancy, and interstitial defects; e.g. the Li atom substitutes at the Mg site ($Mg_{63}Si_{32}Li_1$). We have also assumed that defects are isolated and do not interact with each other.

The $\Gamma-$ centered ($2 \times 2 \times 2$) $k-$ point mesh was sampled for charge density integration over the Brillouin zone of the supercell. The atomic positions were fully relaxed until the magnitude of the remining forces was lower than 0.005 eV Å^{-1}. We do not include the spin–orbital interaction (SOI) when computing total energies, to avoid the huge computational cost.

The charged defect formation energy of a defect D in the charge state q (D^q) in Mg_2X was calculated using the following equation [25, 27, 36]:

$$E_{\mathrm{form}}\left(E_{\mathrm{F}},\ D^q,\ \mathrm{Mg}_2X\right) = E_{\mathrm{tot}}\left[D^q\right] - E_0 - \sum_j \left(\mu_j \Delta n_j\right) + qE_{\mathrm{F}} + E_{\mathrm{corr}} \tag{1}$$

where $E_{\mathrm{tot}}[D^q]$ and E_0 are the total energies with and without defect in the supercell, j is the atomic species in the supercell, Δn_j is the number change of atomic species in the supercell with respect to the pristine supercell without defects, and q is an integer number ($q=$ 2+, 1+, 0, 1−, 2−). E_{F} is the electron Fermi level. E_{corr} is the correction term for the charged-defect supercell calculations [37] for which we followed the Freysoldt–Neugebauer–Van de Walle (FNV) correction method [38]. For the FNV correction, we computed the dielectric constant using the density-functional perturbation theory and obtained the following values: 12.0 for Mg_2Si and 18.9 for Mg_2Sn. Here, we have calculated E_{corr} only for Li-related defects.

The following point defects were considered: Mg vacancy (V_{Mg}), X vacancy (V_x), Mg interstitial (Mg_{int}), X interstitial (X_{int}), X on Mg site (X_{Mg}), and Mg on X site (Mg_x), Li on Mg site (Li_{Mg}) and Li interstitial (Li_{int}, on the 4b site). The atomic chemical potentials and charged defect formation energies were calculated under Mg_2Si(Mg_2Sn)-, Si(Sn)-, and LiSi(LiSn)-rich conditions. As in our case, $\mu_{\mathrm{Si}} = \mathrm{E}_{\mathrm{Si(fcc)}}$ was used from FCC Si, while for $\mu_{\mathrm{Mg}} = 0.5\left(\mathrm{E}_{\mathrm{Mg_2Si}} - \mathrm{E}_{\mathrm{Si(fcc)}}\right)$. Furthermore, the chemical potential of Li (μ_{Li}) is calculated from a LiSi-rich condition where $\mu_{\mathrm{Li}} = \mathrm{E}_{\mathrm{LiSi}} - \mu_{\mathrm{Si}}$. Similarly, for the defects in Mg_2Sn, $\mu_{\mathrm{Li}} = \mathrm{E}_{\mathrm{LiSn}} - \mu_{\mathrm{Sn}}$ and $\mu_{\mathrm{Sn}} = \mathrm{E}_{\beta-\mathrm{Sn}}$ were used from β-Sn.

There are several Li_xSi phases. We have used the $x = 1$ phase due to the experimentally observed formation [39] and because it has the lowest Li atomic chemical potential among Li_xSi.

The the band gap size is crucial for defect properties in semiconductors. Therefore we used hybrid-DFT calculations to obtain the band gaps of Mg_2Si and Mg_2Sn. Note that non-hybrid DFT calculations severely underestimate the corresponding band gaps [40].

We have also calculated the Fermi level at finite temperature as the electrons in materials can be thermally activated, in this case, at the sintering temperature (T_{sinter}). The hole carrier density and electron density (n) are determined when the Fermi level (E_{F}) and temperature are given [36]:

$$n - p = \int_0^{\infty} g(E) \cdot f(E)\,\mathrm{d}E \tag{2}$$

where $g(E)$ is the density of states (DOS) and $f(E)$ is the Fermi–Dirac distribution $f(E) = 1/\left(\exp\left(\frac{E-E_{\mathrm{F}}}{k_{\mathrm{B}}T_{\mathrm{sinter}}}\right)+1\right)$. The $g(E)$ is calculated using DFT-PBE with SOI while the bandgap is corrected using the hybrid-DFT, following previous work [27]. Note that the inclusion of SOI in the Mg_2X system plays a crucial role in the TE transport coefficient and DOS due to its significant effect on band dispersions [41].

Since the whole system should be charge-neutral, the total charge densities from free carriers and defect densities should be zero. From this charge-neutrality condition follows:

$$n - p = \sum_{D,q} q \cdot n\left(D^q\right);\ n\left(D^q\right) \cong n_{\mathrm{latt}}\theta_{\mathrm{deg}}\exp\left(-\frac{E_{\mathrm{Form}}\left(D^q\right)}{k_B T_{\mathrm{sinter}}}\right) \tag{3}$$

where n_{latt} is the number density of available lattice sites in materials, θ_{deg} is the number of degrees of internal freedom of defect on lattice site. The Fermi level and defect densities can thus be obtained by solving equations (2) and (3) iteratively. Here we have corrected the Li-defect density by normalizing the Li doping density if the defect density exceeds the doping density. This is a reasonable approach because Boltzmann factor assumes the relative population density between states. Note that we assume for the comparison between experimental and calculated results that the defect densities are determined by the processing step at the highest temperature (here T_{sinter}) but remain temperature independent afterwards, due to the quenching of the samples. Hence the $n - p$ values are also considered to be temperature independent.

3. Results

Figure 1 shows carrier concentration and dopant efficiency for the samples of $Mg_{2-y}Li_ySi_{1-x}Sn_x$ discussed in [28, 29]. It can be seen that the carrier concentration and dopant efficiency increase with higher Sn content by more than two orders of magnitude. Furthermore, except for $y = 0.005,\ 0.01$ and $x = 0.8$ and 1, a clear decrease in dopant efficiency with increasing Li concentration and Si content can be observed. It is plausible that the trends of dopant concentration with x and y are related to the interplay of the Li-related defects, in particular $\frac{c_{Li_{Mg}}}{c_{Li_{int}}}$ [25].

Figure 2 shows defect formation energy curves for intrinsic and Li-related defects in Mg-poor Mg_2Si and Mg_2Sn in the range of -1 to 1 eV [25]. As the formation energies of the intrinsic defects are significantly higher around the valence band maximum (VBM) and the conduction band minimum (CBM), they can be neglected in the following. We discuss only the Mg-poor case since the samples were synthesized with no Mg excess, and Mg losses during the synthesis are likely, note that equation (1) will vary in dependence on Mg-rich or -depleted conditions. Furthermore, if a significant fraction of the Li does not substitute Mg but goes onto the interstitial position, this would further increase the effective Mg deficiency. Based on the hybrid-DFT calculation, the band gaps of Mg_2Si and Mg_2Sn were estimated to be 0.57 eV and 0.145 eV [25, 40], respectively. The Fermi level is determined by the charge-neutrality equation balancing charged defect densities and free charge carriers and determines the transport properties. It is not easily experimentally accessible, however, due to the exponential energy dependence of defect densities, the Fermi level is often close to the crossing point of the formation energies of the two lowest lying defects E_{cross} [27, 35, 37, 42, 43]. For Mg_2Si and Mg_2Sn these are Li_{Mg} and Li_{int}, where Li_{Mg} is an acceptor defect and the extrinsic defect behind highly doped p-type Mg_2X: see figures S1 and S2 in the SI. However, Li_{int} is more stable than Li_{Mg} deep in the valence band (VB) and up to -0.272 eV and -0.241 eV for Mg_2Si and Mg_2Sn with respect to the CBM, respectively, overcompensating the acceptor effect of Li_{Mg} in this region and pinning the Fermi level around the crossing point. For Li-doped Mg_2Si under Mg-poor conditions, the crossing point of the lowest-lying (and thus highest concentrated) defects is quite precisely in the middle of the bandgap, indicating that obtaining a strong p-type doping effect is impossible. However, for Li-doped Mg_2Sn, the Fermi level can be pinned inside the VB as the crossing point is inside the VB where Li_{Mg} is a neutral defect, $q = 0$. Thus, Li doping can induce p-type conduction due to the narrow bandgap for Mg_2Sn. As was shown in a previous work, the main difference between the two materials is that the position of the VBM with respect to vacuum energy decreases approximately linearly with increasing Sn content from Mg_2Si to Mg_2Sn [27, 44], while, the position of the CBM is more or less the same for Mg_2Si and Mg_2Sn.

Here, we translate the hybrid-DFT data into values comparable with the experimental data. In particular, we estimate the expected maximum achievable carrier concentration using the SPB model approximating the Fermi level by E_{cross} and compare it with the measured carrier concentration. In addition, the Fermi level is obtained solving the charge-neutrality equation (see equations (2) and (3)) using the full band structure as obtained by hybrid DFT band gap corrected DFT + SOI band structures.

The predicted carrier concentration (p_{SPB}) can be determined using a SPB model, given by $p_{SPB} = 4\pi\left(\frac{2m_D^*k_BT}{h^2}\right)^{1.5}F_{0.5}(\eta)$, where m_D^* is the density of states effective mass, k_B is the Boltzmann constant, $F_i(\eta)$ is the Fermi integral of order i and the reduced chemical potential (η) is given by $\eta = \frac{E_{cross}}{k_BT}$. m_D^* is obtained from the experimental data. T is taken as the sintering temperature of the samples. The crossing point for holes ($E_{cross,\ h}$) is at ~ -0.30 eV for Mg_2Si (inside the band gap) and at $\sim +0.095$ eV for Mg_2Sn; note that we have taken the value of $E_{cross,h}$ with respect to the VBM and that the energy direction is opposite to that of figure 2 ($E_{cross,h} = E_{VBM} - E_{cross,e}$), where $E_{cross,e}$ is the energy of the crossing point as displayed in figure 2), as we are considering a p-type material here. The parameters and the results are listed in table 1.

The energy of the crossing point ($E_{cross,h} = -0.30$ eV) is slightly different from the Fermi level calculated using the CN equation ($E_{F,h} = -0.33$ eV) for Mg_2Si. In the case of Mg_2Sn, the values are different by 0.065 eV and closer to the VBM. Overall, the agreement between $E_{cross,h}$ and $E_{F,h}$ is not too bad. The crossing

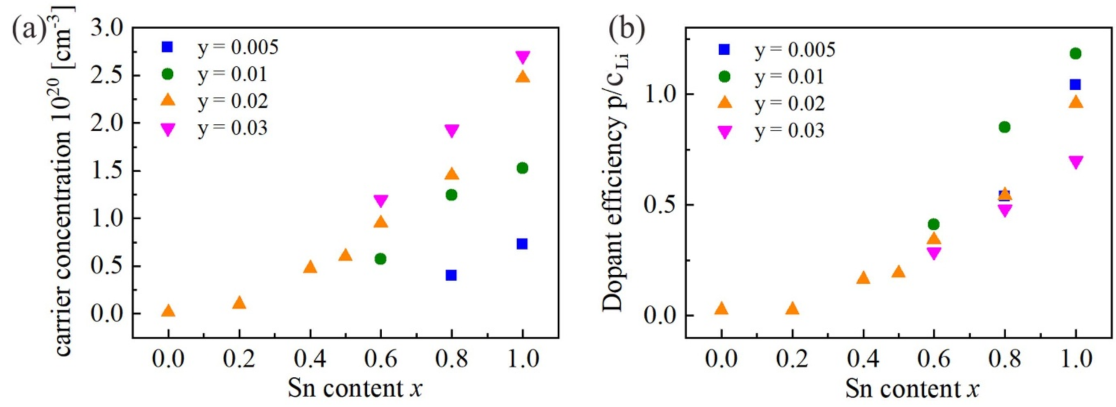

Figure 1. (a) Carrier concentration and (b) dopant efficiency $\left(\frac{p}{c_{\text{Li}}}\right)$ for the whole series of solid solutions of p-type Mg_{2}-$_{y}$Li$_{y}$Si1-$_{x}$Sn$_{x}$ with $0 < x < 1$ and $y = 0.05, 0.01, 0.02,$ and 0.03 at room temperature. Carrier concentration increases with higher Li concentration and Sn content while the dopant efficiency increases with Sn content but decreases with increasing Li concentration.

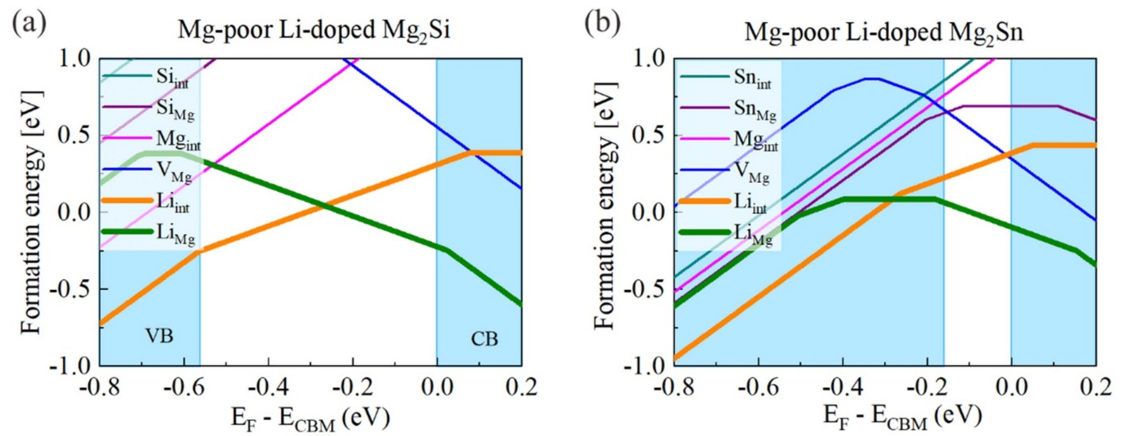

Figure 2. Charged defect formation energy curves for (a) Li-related defects in Mg-poor Mg_2Si and (b) Mg-poor Mg_2Sn at 0 K. White regions indicate the bandgap. The figure was composed using the defect formation energies as those published in [25, 27], except for the Li-related defects for which a correction term for the charged-defect supercell calculations was considered here.

Table 1. Input parameters for the SPB model to calculate carrier concentrations of Mg-poor Li-doped Mg_2Si and Mg_2Sn. In addition, the hybrid-DFT results of the predicted Fermi level and carrier concentration for Mg_2Si at 1073 K and Mg_2Sn at 873 K, respectively. Note that (reduced) energies are given by $E_{\text{cross},h} = E_{\text{VBM}} - E_{\text{cross},e}$ for a p-type material.

Parameters	Mg_2Si	Mg_2Sn
$E_{\text{cross,e}}$ [eV]	~ -0.27	~ -0.24
$E_{\text{cross,h}}$ [eV]	~ -0.30	$\sim +0.095$
m^*_{D} [m_0]	2.2	1.1
p_{SPB} [cm^{-3}]	2.13×10^{19}	2.67×10^{20}
η	–3.24	1.26
$p_{\text{max, exp}}$ [cm^{-3}]	1.52×10^{18}	2.7×10^{20}
T [K]	1073	873
$E_{\text{F,h}}$ (from equation (2)) [eV]	—0.33	+0.03
$p - n$ [cm^{-3}]	—3.3 $\times 10^{17}$ (n-type)	6.1×10^{19}

point E_{cross}, which is directly available from the defect formation energy plots, might therefore be used as a rough guess to estimate carrier concentrations.

For Mg_2Si, the predicted carrier concentration using the SPB model (p_{SPB}) is overestimated compared to the measured carrier concentration ($p_{\text{max,exp}}$), $\frac{p_{\text{SPB}}}{p_{\text{max,exp}}} \approx 14$, while $(p - n) \approx p_{\text{CN}}$ is negative (n-type) in disagreement with our experimental result (p-type). Note that while solving equations (2) and (3) gives actually $p - n$, this is essentially p at room temperature. On the other hand, Mg_2Sn shows good agreement between $p_{\text{max,exp}}$ and p_{SPB} ($\frac{p_{\text{SPB}}}{p_{\text{max,exp}}} \approx 1$), while the difference is larger for $p_{\text{max,exp}}$ and p_{CN} ($\frac{p_{\text{max,exp}}}{p_{\text{CN}}} \approx 4.4$).

Table 2. The predicted carrier concentration and dopant efficiency from solving the charge-neutrality equation for $Mg_{2-y}Li_ySn$ with $y = 0.005, 0.01$ and 0.03 at 873 K, using first-principles results.

$Mg_{2-y}Li_ySn$	p_{CN} (cm^{-3})	Li dopant efficiency $\frac{p}{c_{Li}}$
$y =$ 0.005	3.4×10^{19}	0.53
$y =$ 0.01	4.5×10^{19}	0.35
$y =$ 0.03	6.1×10^{19}	0.16

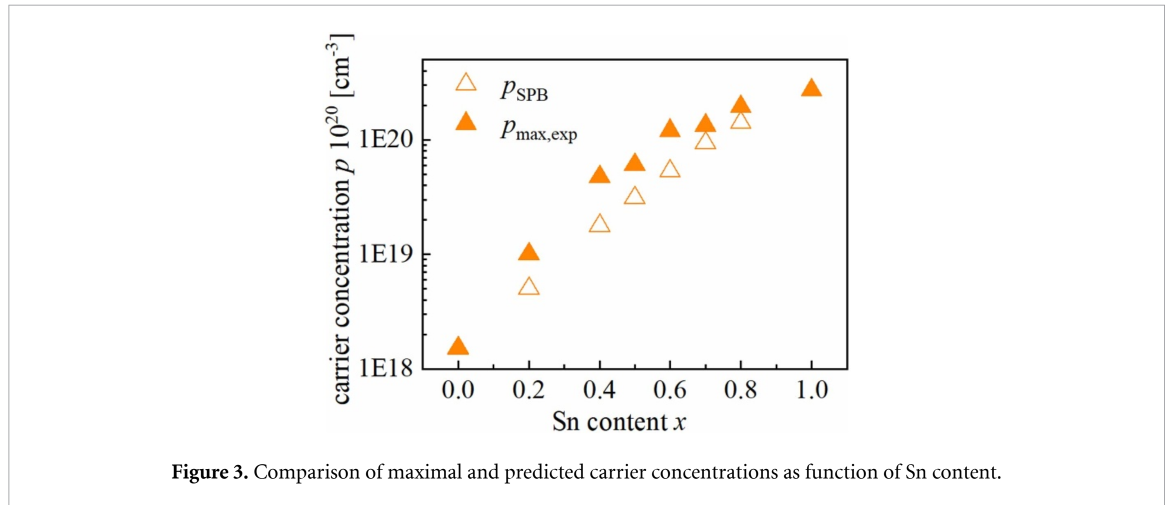

Figure 3. Comparison of maximal and predicted carrier concentrations as function of Sn content.

Table 2 shows the predicted carrier concentration and dopant efficiency for Mg_2Sn with different Li concentrations from solving the CN equation using the first-principles results. p_{CN} increases while the dopant efficiency decreases with higher Li concentrations. This is in agreement with the experimental data in figure 1.

While the hybrid-DFT predicts the trends in carrier concentration and dopant efficiency for the binaries in agreement with experimental results, agreement in absolute numbers might not be expected and is not observed. To predict the maximal achievable carrier concentration for the solid solutions we therefore do not only rely on hybrid-DFT calculations, which are feasible but require substantial effort. Instead, we have used the SPB model to predict the maximal carrier concentration in p-Mg_2(Si, Sn) based on an interpolation of the hybrid-DFT results as follows: first, we have adjusted $E_{cross,h}$ such that the predicted p, by using the SPB model, equals the experimental result for $x = 0$ and 1. As discussed above, this is in good agreement with the result of the hybrid-DFT calculation for Mg_2Sn, but not for Mg_2Si, as minority carriers cannot be neglected. Second, we have assumed that $E_{cross,h}$ varies linearly for the solid solutions ($E_{cross,h} = -0.5453 + 0.6415x$). A linear interpolation of the sintering temperature ($T_{sinter} = 873 - 1073$ K) was employed to calculate the reduced chemical potential and the respective carrier concentration. We have assumed that Li distributes similarly in the binaries as well as in the solid solution; in particular, that it does not show preferential accumulation around either Si or Sn. This assumption is justified by the very similar electronegativities of Si and Sn (Si = 1.90, Sn = 1.96) [45] and provides some base for a linear interpolation from the binaries to the ternaries.

Despite the massive simplifications (linear interpolation, assumption of SPB model for Mg_2Si), the predicted carrier concentrations agree with the experimental maxima quite well as shown in figure 3; the maximum deviation is a factor of $\sim$2.7. Thus, all in all, we have a rough model to estimate the maximum carrier concentrations for the whole Mg_2(Si, Sn) solid solution range.

4. Discussions

The observed experimental carrier concentration and dopant efficiencies are comparable with the previous results in [24, 46–48] for the Sn-rich compositions; the carrier concentration increased with increasing Li and Sn content. There is significant scatter within the experimental data in literature as synthesis routes and synthesis parameters (times, sintering temperatures) differ. In particular, for Li-doped $Mg_2Si_{0.4}Sn_{0.6}$, Tang *et al* reported higher carrier concentration in comparison to us and previous literature [24, 46–48]. Nevertheless, even there, a dopant efficiency <0.5 is observed. A change in Mg chemical potential can explain partially the scatter in carrier concentrations.

The trend of increasing carrier concentration with higher Sn content can be understood from the interplay between Fermi level and density of states or effective mass. Similar DOS shape and values for the VB have been reported [29, 45, 49, 50], our results using hybrid-DFT, and with an exact-exchange mixing parameter of 25%, are shown in figures S1 and S2 of the SI. However, the VB-DOS close to the band edge differs between the two binaries, which determines the transport properties via the density of states effective mass (m_D^*). Thus, in this case, alloying elements change the band edge of VB gradually and the density of states effective mass decreases towards Mg_2Sn. On the other hand, with respect to the dopant, a negligible effect of Li on the DOS of the VB for Mg_2Si and the $Mg_2Si_{0.25}Sn_{0.75}$, and hence on the effective mass, has been reported [29, 47], also in agreement with our findings (figures S1 and S2). Thus, for a fixed crossing point or Fermi level, the VB curvature influences the resulting carrier concentration and this is captured by the employed effective mass. However, even though the m_D^* for Mg_2Sn is smaller than Mg_2Si with $\frac{m^*_{DMg2Sn}}{m^*_{DMg2Si}} \approx \frac{1}{2}$, the carrier concentration is higher for Mg_2Sn than for Mg_2Si because the crossing point (and hence the Fermi level) for Mg_2Sn is at a much higher value (on the hole energy axis).

We have observed that the SPB-predicted carrier concentration of p-type Mg_2Si is overestimated compared to the observed carrier concentration. In this case, the use of the SPB model is far from ideal as the crossing point is deep inside the band gap. Therefore, employing a two-band model is expected to yield closer agreement for p-type Mg_2Si. For Mg_2Sn, on the other hand, the agreement between carrier concentration from DFT and SPB is much better, partially because the crossing point is inside the VB indicating that Li-doped Mg_2Sn is a degenerate semiconductor. The quantitative disagreement between experimental data and DFT predictions is partially due to inaccuracies of the DFT calculations in band edge positions, DOS effective masses, and computed defect formation energies. While, if employed correctly, DFT can be used to predict trends with good reliability the absolute inaccuracy in e.g. band maxima position can easily be in the range of $0.01 - 0.1$ eV, translating in significant errors for defect and carrier concentrations due to the exponential dependencies. Further inaccuracies may arise from supercell approximation: as in our case, we have a supercell with 96 atoms, which might be considered to be a small supercell [51]. Also we assume that all defects are non-interacting point defects, which would be inexact in the high-defect density regime. The vibrational entropy and temperature dependent lattice and band gap also would affect the charged defect formation energies and DOSs [37] which will shift the Fermi level and change the doping efficiency. In addition to that, the choice of exchange-correlation energy functional would affect the band gap correction and the defect total energy, hence resulting in the slight change in the defect formation energies [35]. Note also that, in this stage, our DFT-based carrier concentration prediction does not consider the experimentally observed reduction of the band gap with temperature [4, 52]. We also assumed thermodynamic equilibrium for the defect generation, and have assumed them to be quenched in the following, not considering further evolution of these meta stable states. In essence, a combination of the DFT results for the defect formation energies and a simple SPB model can serve as a rough guide for experimentalists in predicting the maximum achievable carrier concentration for the solid solutions.

It is worth considering whether the conclusions for Li can be transferred to other dopants as a low dopant efficiency is observed universally in p-type $Mg_2Si_{1-x}Sn_x$ [6]. We note that e.g. for Ag the situation with respect to the extrinsic defects is comparable to that of Li: the two relevant and compensating defects Ag_{Mg} and Ag_{int} also have their crossing point in the gap for Mg_2Si. For Mg_2Sn the same trend is expected as the Ag_{Mg} defect is predicted to become neutral for $E < -0.228$ eV. Thus a similar trend with Si:Sn and dopant amount can be expected, albeit on a lower level of carrier concentration. In addition a limited and possibly Si:Sn-dependent solubility of Ag might impose further restrictions [6, 17, 18, 20], different to Li, were a high solubility has been observed [23].

We have furthermore transferred our approach of using the crossing point from the charged defect formation energies diagram in combination with an SPB model to other material systems. The materials Na-, K-, Ag-doped PbSe [53] and Te doped Mg_3Sb_2 [54] were chosen based on the availability of defect formation energy diagrams. The input parameters (E_{cross} and m_D^*) are taken from the cited literature and the highest synthesis T and sintering T are considered for the calculation of PbSe and Mg_3Sb_2, respectively [53–55]; for Mg_3Sb_2, the Fermi level is at the reported Te solubility limit which is inside the CB and not at the crossing point. The results revealed that our approach is transferable to these material systems with a factor of three being the maximal difference between experimental and predicted carrier concentration (see figure 4). This somewhat large discrepancy in $Ag_xPb_{1-x}Se$ is possibly because of the variation in the density of states effective masses [56]. In this case, the m_D^* is dependent on the carrier concentration, which is not covered by the employed SPB model.

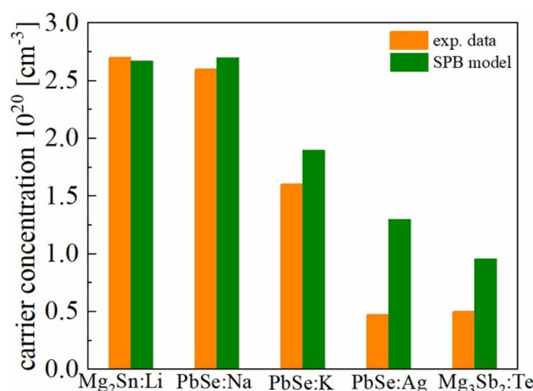

Figure 4. Comparison of maximal and predicted carrier concentrations in Mg_2Sn (our work), $Na_xPb_{1-x}Se$ [53], $K_xPb_{1-x}Se$ [53], $Ag_xPb_{1-x}Se$ [53], and Mg_3Sb_2 [54]. Experimental parameters are taken from [53–55], while the calculated results were obtained using a procedure analog to that presented here for Mg_2Sn.

5. Conclusion

In this work, we analyze the experimental data for Li-doped Mg_2Si-Mg_2Sn solid solutions; the carrier concentration increases with higher Li content, but the dopant efficiency decreases. With increasing Sn content, the carrier concentration and the dopant efficiency increase. The crossing point of the lowest-lying defect formation energies from hybrid DFT, which corresponds approximately to the Fermi level, can explain the observed trend. Further, we show that a linear interpolation of the Fermi level from the crossing point between Mg_2Si and Mg_2Sn and a simple SPB model can be used to predict the maximal achievable carrier concentration for the solid solutions, in good agreement with the experimental data. This work thus shows that consideration of intrinsic and extrinsic defects is crucial for the optimization of TE materials and that DFT-based defect formation energies can be used to understand experimentally-observed trends.

Data availability statement

All data that support the findings of this study are included within the article (and any supplementary files).

Acknowledgments

The authors would like to gratefully acknowledge the endorsement from the DLR Executive Board Members for Space Research and Technology and the financial support from the Young Research Group Leader Program. The authors (H K and A S) would like to acknowledge financial support by the DAAD (Fellowships no. 247). J de Boor also acknowledges support by the Deutsche Forschungsgemeinschaft (DFG, German Research Foundation)—Project Number 396709363.

This work was also supported by the Korea Institute of Energy Technology Evaluation and Planning (KETEP) funded by the Ministry of Trade, Industry & Energy (MOTIE), Republic of Korea: Grant No. 20188550000290. The author from the Korea Electrotechnology Research Institute (KERI) was also supported by the KERI Primary Research Program through the National Research Council of Science and Technology (NST) funded by the Ministry of Science and ICT (MSIT) of the Republic of Korea: Grant No. 22A01008.

Conflict of interest

The authors have no conflicts to declare.

ORCID iDs

Hasbuna Kamila https://orcid.org/0000-0001-8959-392X

Byungki Ryu https://orcid.org/0000-0002-0867-6457

Aryan Sankhla https://orcid.org/0000-0002-1527-6902

Johannes de Boor https://orcid.org/0000-0002-1868-3167

References

[1] Sankhla A, Patil A, Kamila H, Yasseri M, Farahi N, Mueller E and de Boor J 2018 Mechanical alloying of optimized $Mg_2(Si, Sn)$ solid solutions: understanding phase evolution and tuning synthesis parameters for thermoelectric applications *ACS Appl. Energy Mater.* **1** 531–42

[2] Goyal G K *et al* 2019 High thermoelectric performance in $Mg_2(Si_{0.3}Sn_{0.7})$ by enhanced phonon scattering *ACS Appl. Energy Mater.* **2** 2129–37

[3] Liu W, Tan X, Yin K, Liu H, Tang X, Shi J, Zhang Q and Uher C 2012 Convergence of conduction bands as a means of enhancing thermoelectric performance of n-type $Mg_2Si_{1-x}Sn_x$ solid solutions *Phys. Rev. Lett.* **108** 166601

[4] Zaitsev V K, Fedorov M I, Gurieva E A, Eremin I S, Konstantinov P P, Samunin A Y and Vedernikov M V 2006 Highly effective $Mg_2Si_{1-x}Sn_x$ thermoelectrics *Phys. Rev.* B **74** 045207

[5] Liu W *et al* 2015 n-type thermoelectric material $Mg_2Sn_{0.75}Ge_{0.25}$ for high power generation *Proc. Natl Acad. Sci.* **112** 3269–74

[6] de Boor J, Dasgupta T, Saparamadu U, Mueller E and Ren Z F 2017 Recent progress in p-type thermoelectric magnesium silicide based solid solutions *Mater. Today Energy* **4** 105–21

[7] Gao P, Berkun I, Schmidt R D, Luzenski M F, Lu X, Bordon Sarac P, Case E D and Hogan T P 2014 Transport and mechanical properties of high-ZT $Mg_{2.08}Si_{0.4-x}Sn_{0.6}Sb_x$ thermoelectric materials *J. Electron. Mater.* **43** 1790–803

[8] Kamila H, Sahu P, Sankhla A, Yasseri M, Pham H-N, Dasgupta T, Mueller E and de Boor J 2019 Analyzing transport properties of p-type Mg_2Si–Mg_2Sn solid solutions: optimization of thermoelectric performance and insight into the electronic band structure *J. Mater. Chem.* A **7** 1045–54

[9] Naithani H, Mueller E and de Boor J 2022 Developing a two-parabolic band model for thermoelectric transport modelling using Mg_2Sn as example *j. phys. energy* (under revision)

[10] Tumminello S, Ayachi S, Fries S G, Mueller E and de Boor J 2021 Applications of thermodynamic calculations to practical TEG design: $Mg_2(Si_{0.3}Sn_{0.7})$/Cu interconnections *J. Mater. Chem.* A **9** 20436–52

[11] Castillo-Hernández G, Mueller E and de Boor J 2022 Impact of the dopant species on the thermomechanical material properties of thermoelectric $Mg_2Si_{0.3}Sn_{0.7}$ *Materials* **15** 779

[12] Nakamura T, Hatakeyama K, Minowa M, Mito Y, Arai K, Iida T and Nishio K 2015 Power-generation performance of a π-structured thermoelectric module containing Mg_2Si and $MnSi_{1.73}$ *J. Electron. Mater.* **44** 3592–7

[13] de Boor J, Dasgupta T and Mueller E 2016 Thermoelectric properties of magnesium silicide–based solid solutions and higher manganese silicides *Materials Aspect of Thermoelectricity* (Boca Raton, FL: CRC Press Taylor & Francis Group) pp 159–218

[14] Saparamadu U, Mao J, Dahal K, Zhang H, Tian F, Song S, Liu W and Ren Z 2017 The effect of charge carrier and doping site on thermoelectric properties of $Mg_2Sn_{0.75}Ge_{0.25}$ *Acta Mater.* **124** 528–35

[15] Liu X *et al* 2013 Low electron scattering potentials in high performance $Mg_2Si_{0.45}Sn_{0.55}$ based thermoelectric solid solutions with band convergence *Adv. Energy Mat.* **3** 1238–44

[16] de Boor J, Gupta S, Kolb H, Dasgupta T and Mueller E 2015 Thermoelectric transport and microstructure of optimized $Mg_2Si_{0.8}Sn_{0.2}$ *J. Mater. Chem.* C **3** 10467–75

[17] Chen H Y, Savvides N, Dasgupta T, Stiewe C and Mueller E 2010 Electronic and thermal transport properties of Mg_2Sn crystals containing finely dispersed eutectic structures *Phys. Status Solidi* a **207** 2523–31

[18] Chen H Y and Savvides N 2010 High quality Mg_2Sn crystals prepared by RF induction melting *J. Cryst. Growth* **312** 2328–34

[19] Chen H Y and Savvides N 2009 Microstructure and thermoelectric properties of n- and p-type doped Mg_2Sn compounds prepared by the modified bridgman method *J. Electron. Mater.* **38** 1056–60

[20] Savvides N and Chen H Y 2010 Thermal conductivity and other transport properties of Mg_2Sn: AgCrystals *J. Electron. Mater.* **39** 2136–41

[21] Saparamadu U, de Boor J, Mao J, Song S, Tian F, Liu W, Zhang Q and Ren Z 2017 Comparative studies on thermoelectric properties of p-type $Mg_2Sn_{0.75}Ge_{0.25}$ doped with lithium, sodium, and gallium *Acta Mater.* **141** 154–62

[22] Ihou-Mouko H, Mercier C, Tobola J, Pont G and Scherrer H 2011 Thermoelectric properties and electronic structure of p-type Mg_2Si and $Mg_2Si_{0.6}Ge_{0.4}$ compounds doped with Ga *J. Alloys Compd.* **509** 6503–8

[23] Nieroda P, Kolezynski A, Oszajca M, Milczarek J and Wojciechowski K T 2016 Structural and thermoelectric properties of polycrystalline p-type $Mg_{2-x}Li_xSi$ *J. Electron. Mater.* **45** 3418–26

[24] Gao P, Davis J D, Poltavets V V and Hogan T P 2016 The p-type $Mg_2Li_xSi_{0.4}Sn_{0.6}$ thermoelectric materials synthesized by a B_2O_3 encapsulation method using Li_2CO_3 as the doping agent *J. Mater. Chem.* C **4** 929–34

[25] Ayachi S *et al* 2020 On the relevance of point defects for the selection of contacting electrodes: Ag as an example for $Mg_2(Si,Sn)$-based thermoelectric generators *Mater. Today Phys.* **20** 100309

[26] Hirayama N, Iida T, Sakamoto M, Nishio K and Hamada N 2019 Substitutional and interstitial impurity p-type doping of thermoelectric Mg_2Si: a theoretical study *Sci. Technol. Adv. Mater.* **20** 160–72

[27] Ryu B, Choi E-A, Park S, Chung J, de Boor J, Ziolkowski P, Müller E and Park S 2021 Native point defects and low p-doping efficiency in $Mg_2(Si,Sn)$ solid solutions: a hybrid-density functional study *J. Alloys Compd.* **853** 157145

[28] Kamila H *et al* 2019 Synthesis of p-type $Mg_2Si_{1-x}Sn_x$ with $x = 0$–1 and optimization of the synthesis parameters *Mater. Today: Proc.* **8** 546–55

[29] de Boor J, Berche A and Jund P 2020 Density of states effective mass for p-type Mg_2Si–Mg_2Sn solid solutions: comparison between experiments and first-principles calculations *J. Phys. Chem.* C **124** 14987–96

[30] Kamila H, Goyal G K, Sankhla A, Ponnusamy P, Mueller E, Dasgupta T and de Boor J 2019 Systematic analysis of the interplay between synthesis route, microstructure, and thermoelectric performance in p-type $Mg_2Si_{0.2}Sn_{0.8}$ *Mater. Today Phys.* **9** 100133

[31] Krukau A V, Vydrov O A, Izmaylov A F and Scuseria G E 2006 Influence of the exchange screening parameter on the performance of screened hybrid functionals *J. Chem. Phys.* **125** 224106

[32] Kresse G and Joubert D 1999 From ultrasoft pseudopotentials to the projector augmented-wave method *Phys. Rev.* B **59** 1758–75

[33] Kresse G and Furthmüller J 1996 Efficient iterative schemes for *ab initio* total-energy calculations using a plane-wave basis set *Phys. Rev.* B **54** 11169–86

[34] Perdew J P, Burke K and Ernzerhof M 1996 Generalized gradient approximation made simple *Phys. Rev. Lett.* **77** 3865–8

[35] Toriyama M, Brod M and Snyder G J 2021 Chemical interpretation of charged point defects in semiconductors: a case study of Mg_2Si (https://doi.org/10.26434/chemrxiv-2021-729bm)

[36] Zhang S B and Northrup J E 1991 Chemical potential dependence of defect formation energies in GaAs: application to Ga self-diffusion *Phys. Rev. Lett.* **67** 2339–42

[37] Freysoldt C, Grabowski B, Hickel T, Neugebauer J, Kresse G, Janotti A and Van de Walle C G 2014 First-principles calculations for point defects in solids *Rev. Mod. Phys.* **86** 253–305
[38] Freysoldt C, Neugebauer J and Van de Walle C G 2009 Fully *Ab initio* finite-size corrections for charged-defect supercell calculations *Phys. Rev. Lett.* **102** 016402
[39] Tang W S, Chotard J-N and Janot R 2013 Synthesis of single-phase LiSi by ball-milling: electrochemical behavior and hydrogenation properties *J. Electrochem. Soc.* **160** A1232–40
[40] Ryu B, Park S, Choi E-A, de Boor J, Ziolkowski P, Chung J and Park S D 2019 Hybrid-functional and quasi-particle calculations of band structures of Mg_2Si, Mg_2Ge, and Mg_2Sn *J. Korean Phys. Soc.* **75** 144–52
[41] Kutorasinski K, Wiendlocha B, Tobola J and Kaprzyk S 2014 Importance of relativistic effects in electronic structure and thermopower calculations for Mg_2Si, Mg_2Ge, and Mg_2Sn *Phys. Rev.* B **89** 115205
[42] Goyal A, Gorai P, Anand S, Toberer E S, Snyder G J and Stevanović V 2020 On the dopability of semiconductors and governing material properties *Chem. Mater.* **32** 4467–80
[43] Goyal A *et al* 2017 First-principles calculation of intrinsic defect chemistry and self-doping in PbTe *npj Comput. Mater.* **3** 1–9
[44] Ryu B, Choi E-A and Park S 2019 Asymmetric band alignment responsible for minority carrier blocking in bulk Mg_2(Si,Ge,Sn) thermoelectric alloys: a first-principles study (ICT)
[45] Bourgeois J *et al* 2013 Study of electron, phonon and crystal stability versus thermoelectric properties in $Mg_2X(X = Si, Sn)$ compounds and their alloys *Funct. Mater. Lett.* **06** 1340005
[46] Tang X *et al* 2016 Ultra rapid fabrication of p-type Li-doped $Mg_2Si_{0.4}Sn_{0.6}$ synthesized by unique melt spinning method *Scr. Mater.* **115** 52–56
[47] Zhang Q *et al* 2014 Low effective mass and carrier concentration optimization for high performance p-type $Mg_{2(1-x)}Li_{2x}Si_{0.3}Sn_{0.7}$ solid solutions *Phys. Chem. Chem. Phys.* **16** 23576–83
[48] de Boor J *et al* 2016 Thermoelectric performance of Li doped, p-type Mg_2(Ge,Sn) and comparison with Mg_2(Si,Sn) *Acta Mater.* **120** 273–80
[49] Boulet P and Record M-C 2011 Influence of the modified Becke-Johnson exchange potential on thermoelectric properties: application to Mg_2Si *J. Chem. Phys.* **135** 234702
[50] Jin Y R *et al* 2016 Mg_2Sn: a potential mid-temperature thermoelectric material *RSC Adv.* **6** 48728–36
[51] Komsa H-P and Pasquarello A 2013 Finite-size supercell correction for charged defects at surfaces and interfaces *Phys. Rev. Lett.* **110** 095505
[52] Bahk J-H, Bian Z and Shakouri A 2014 Electron transport modeling and energy filtering for efficient thermoelectric $Mg_2Si_{1-x}Sn_x$ solid solutions *Phys. Rev.* B **89** 075204
[53] Grovogui J A, Slade T J, Hao S, Wolverton C, Kanatzidis M G and Dravid V P 2021 Implications of doping on microstructure, processing, and thermoelectric performance: the case of PbSe *J. Mater. Res.* **36** 1272–84
[54] Ohno S *et al* 2018 Phase boundary mapping to obtain n-type Mg_3Sb_2-based thermoelectrics *Joule* **2** 141–54
[55] Wang H *et al* 2011 Heavily doped p-type PbSe with high thermoelectric performance: an alternative for PbTe *Adv. Mater.* **23** 1366–70
[56] Wang S *et al* 2011 Exploring the doping effects of Ag in p-type PbSe compounds with enhanced thermoelectric performance *J. Phys. D: Appl. Phys.* **44** 475304